

**Determination of geochronology and sedimentation rates of shallow lakes in the middle Yangtze reaches using  $^{210}\text{Pb}$ ,  $^{137}\text{Cs}$  and spheroidal carbonaceous particles**

Xu Chen<sup>1\*</sup>, Qianglong Qiao<sup>1</sup>, Suzanne McGowan<sup>2</sup>, Linghan Zeng<sup>1,2</sup>, Mark A Stevenson<sup>3</sup>, Lei Xu<sup>1</sup>, Chunling Huang<sup>1</sup>, Jia Liang<sup>1</sup>, Yanmin Cao<sup>4</sup>

<sup>1</sup>State Key Laboratory of Biogeology and Environmental Geology, School of Earth Sciences, China University of Geosciences, Wuhan 430074, China

<sup>2</sup>School of Geography, University of Nottingham, Nottingham NG7 2RD, UK

<sup>3</sup>School of Natural and Environmental Sciences, Newcastle University, Newcastle-upon-Tyne NE1 7RU, UK

<sup>4</sup>College of Resources and Environmental Science, South-Central University for Nationalities, Wuhan 430074, China

\*Corresponding author; e-mail address: xuchen@cug.edu.cn

**<https://doi.org/10.1016/j.catena.2018.11.041>**  
**Catena**

**Abstract:** Accurate chronologies for recent sediments of shallow lakes in the Yangtze floodplain are critical to calibrate proxy records for reconstructing environmental changes during the past century. This study presents the results of detailed  $^{210}\text{Pb}$  analysis from eight lake sediment cores collected from the middle Yangtze reaches, southeast China. Unsupported  $^{210}\text{Pb}$  activities generally declined exponentially with mass depth in the eight cores. The chronologies and sedimentation rates for the sediment cores were calculated using different  $^{210}\text{Pb}$ -based mathematical models. The  $^{137}\text{Cs}$  chronomarker (i.e. the 1963 fallout peak) and the spheroidal carbonaceous particle (SCP) chronomarker (i.e. the start of the rapid increase in 1970 AD) were selected to validate the  $^{210}\text{Pb}$  dating. Sedimentation rates derived from different models were validated using historical data including lake area, arable land area, sediment discharge and reservoir volume in the Yangtze basin. The SCP-corrected CRS (constant rate of supply) model performs better than other models, based on validation using historical documents in the Yangtze basin. The  $^{137}\text{Cs}$  chronomarker might be erroneous due to catchment-driven  $^{137}\text{Cs}$  inputs from soil erosion and post-depositional diffusion. Both SCPs and  $^{137}\text{Cs}$  are susceptible to inputs from catchment soil erosion, but SCPs show no apparent degradation and post-depositional changes in lake sediments. The SCP profile provides a relatively reliable chronomarker, which can be used for validating  $^{210}\text{Pb}$  chronologies in these floodplain lakes. Generally, sedimentation rates in the eight lakes were less than  $0.2 \text{ g cm}^{-2} \text{ yr}^{-1}$  before the 1930s, and then increased to a peak in the 1960s. Afterwards, sedimentation rates decreased and remained low after the 1980s.

**Key words:** Lacustrine sediment;  $^{210}\text{Pb}$  radiometric dating; spheroidal carbonaceous particles; multiple dating models; the Yangtze floodplain

## 1. Introduction

Reliably dated lacustrine sediments are crucial archives of past environmental changes, particularly in rapidly developing countries where long-term monitoring data are limited. For dating recent sediments spanning the past 100-150 years,  $^{210}\text{Pb}$  is the most widely used radionuclide with a half-life of 22.26 years (Appleby, 2001; Sanchez-Cabeza and Ruiz-Fernández, 2012).  $^{210}\text{Pb}$  has two main sources in lake sediments, including ‘supported’  $^{210}\text{Pb}$  ( $^{210}\text{Pb}_{\text{sup}}$ ) produced *in situ* by the decay of its parent radionuclide  $^{226}\text{Ra}$  and ‘excess’  $^{210}\text{Pb}$  ( $^{210}\text{Pb}_{\text{ex}}$ ) supplied by the decay of atmospheric  $^{222}\text{Rn}$  (Appleby, 2001). After dry/wet deposition, rapid sedimentation processes remove this radionuclide from the water column into sediments via adsorption onto suspended particles (Krishnaswamy et al., 1971; Mabit et al., 2014).  $^{210}\text{Pb}_{\text{ex}}$  decay rates are predictable based on the half-life, and hence  $^{210}\text{Pb}_{\text{ex}}$  has become widely used for geochronology determination (Appleby, 2001, 2008; Sanchez-Cabeza and Ruiz-Fernández, 2012).

In stable environments with uniform sediment accumulation rates, chronologies based on appropriate dating models are very reliable (Appleby, 2001). For example, in lakes where the sedimentation rate and  $^{210}\text{Pb}_{\text{ex}}$  flux are both constant, the constant flux constant sedimentation model (CFCS) provides reliable dating results (Baskaran et al., 2015; Jweda and Baskaran, 2011; Krishnaswamy et al., 1971). The constant initial concentration model (CIC) assumes a constant initial  $^{210}\text{Pb}_{\text{ex}}$  concentration regardless of any changes in the sedimentation rate (Binford, 1990; Pennington et al., 1976; Robbins and Edgington, 1975). The constant rate of supply model (CRS) assumes a constant flux of  $^{210}\text{Pb}_{\text{ex}}$  to sediment surface and hence that the initial  $^{210}\text{Pb}_{\text{ex}}$  concentration is inversely proportional to the sedimentation rate (Appleby and Oldfield, 1978; Córdoba et al., 2017; Oldfield et al., 1978). Nevertheless, the assumptions and

prerequisites of the commonly used models (e.g. constant initial concentration of  $^{210}\text{Pb}_{\text{ex}}$  and constant sedimentation rate) are not always fulfilled in nature, and hence, different models may produce inconsistent dating results and be more suited to particular environmental circumstances (Baskaran et al., 2015; Córdoba et al., 2017; Lan et al., 2018; Mabit et al., 2014; Tylmann et al., 2013, 2016; von Gunten et al., 2009).

Since it is not known *a priori* which of the models produces the best result, a systematic comparison of different numerical models is vital for establishing accurate chronologies (von Gunten et al., 2009). In addition, the  $^{210}\text{Pb}$  geochronology should be validated using at least one independent tracer which separately provides a clear time-stratigraphic horizon (Smith, 2001; Appleby, 2008). The artificial radionuclide  $^{137}\text{Cs}$  and spheroidal carbonaceous particle (SCP) profiles are widely used to validate  $^{210}\text{Pb}$  chronologies (Appleby, 2001; Rose, 2001). Records of the  $^{137}\text{Cs}$  fallout peak from the atmospheric testing of thermo-nuclear weapons can be used to identify the 1963 depth (Ritchie and McHenry, 1990). SCPs are a component of fly-ash formed by the incomplete high-temperature combustion of fossil fuels, and the characteristics of inert composition, efficient extraction and easy identification make them useful indicators of industrial contamination (Rose, 2001). By comparison with the history of regional industrial activities (e.g. coal consumption), changes in the SCP profile can be used as independent chronomarkers for dating recent sediments (Boyle et al., 1999; Rose, 2001; Wu et al., 2005).

The Yangtze floodplain is a particularly interesting region to study environmental changes during the past century using  $^{210}\text{Pb}$  dating (Boyle et al., 1999; Xiang et al., 2002; Xu et al., 2017; Xue and Yao, 2011). This region is characterized by more than 600 shallow freshwater lakes with surface area  $> 1 \text{ km}^2$  (Wang and Dou, 1998). Paleolimnological studies have revealed that enhanced human activities in the Yangtze

basin (e.g. large-scale deforestation, land reclamation and dam constructions) during the mid-20<sup>th</sup> century have altered the erosional input from the watershed, subsequently changing sedimentation rates as well as the flux of  $^{210}\text{Pb}_{\text{ex}}$  arriving at lake sediment (Xu et al., 2017; Xue and Yao, 2011). For example, in Taibai Lake, sedimentation rate doubled between 1945 and 1953 due to intensive land reclamation at the lake margins (Liu et al., 2012). Previous  $^{210}\text{Pb}$  chronologies of lacustrine sediments in the Yangtze floodplain lakes were mainly derived from the CRS model (Boyle et al., 1999; Du et al., 2001; Xiang et al., 2002; Xu et al., 2017). One dating method alone or single model calculation may result in an over- or under- estimation of the sediment age (Tylmann et al., 2016). In order to validate the robustness of the chronologies, it has been strongly recommended that multiple dating models should be calculated and calibrated with independent chronomarkers (Baskaran et al., 2015; Liu et al., 2009; Smith, 2001; von Gunten et al., 2009).

This study describes the establishment of chronologies for short sediment cores collected from eight shallow lakes of the middle Yangtze reaches. We applied three different dating approaches, i.e.  $^{210}\text{Pb}$ ,  $^{137}\text{Cs}$  and SCP. In order to reveal the range of possible dating results, the  $^{210}\text{Pb}$  chronologies were calculated using five models, i.e. the CIC, CFCS, CRS,  $^{137}\text{Cs}$ -corrected CRS and SCP-corrected CRS models. Sedimentation rates of the eight lakes were calculated and compared to historical documents of arable land area, lake area and sediment discharge from the Yangtze basin. We expected that multiple dating approaches would help to establish reliable chronologies for these shallow floodplain lakes, in comparison with one dating method alone or single model calculation.

## **2 Materials and methods**

## **2.1 Study area**

The Yangtze River ranks third globally in terms of length (6300 km), ninth in catchment area ( $1.8 \times 10^6 \text{ km}^2$ ), fifth in water discharge ( $\sim 900 \text{ km}^3$  per year), and fourth in sediment flux ( $\sim 500$  million tonnes per year, up until 1980) (Chen et al., 2001). The river is generally divided into upper (from the source to Yichang), middle (from Yichang to Hukou) and lower (below Hukou) Yangtze reaches. The Yangtze basin is characterized by a monsoonal climate that features cold, dry winters and hot, wet summers. In the middle Yangtze reaches, mean annual precipitation and mean annual temperature are  $\sim 1200 \text{ mm}$  and  $16\text{-}18 \text{ }^\circ\text{C}$ , respectively. At Yichang and Hankou Stations, annual runoff has been quite stable since 1950; however, sediment discharge has declined markedly since the mid-1980s (Bulletin of Yangtze River sediment, 2003-2015).

The middle Yangtze reaches are characterized by alluvial floodplains, which encompass a number of ecologically and economically valuable lakes and wetlands (Xie et al., 2017). Due to the unique biodiversity, this region has been designated by the World Wide Fund for Nature (WWF) as one of the Global 200 priority ecoregions for conservation (Olson and Dinerstein, 1998). Increasing human disturbances from rapid population growth and economic development in the catchment have caused environmental degradation of these lakes, including surface area shrinkage due to agricultural land reclamation, biodiversity loss and water quality deterioration (Cui et al., 2013; Xie et al., 2017).

## **2.2 Sampling**

Sediment cores were collected from eight lakes between 2011 and 2016 using a gravity corer. Each sediment core was macroscopically described, including lithology,

colour and sedimentary structures, and then sectioned at 1-cm intervals in the field (Fig. 1 and Table 1). The eight lakes include Dongting (DT), Honghu (HH), Luhu (LH), Futou (FT), Shahu (SH), Yanxi (YX), Wanghu (WH) and Poyang (PY) lakes. The sediment samples were transported to the laboratory and stored at 4 °C prior to analyses. Sediment cores from HH and WH have previously been studied for  $^{210}\text{Pb}$  and SCPs, and these cores were collected between 1992 and 1993 (Boyle et al., 1999). In order to retrieve recent environmental change in the two lakes, new cores were collected for further analysis.

### 2.3 Analytical procedures

Radioactive isotopes  $^{210}\text{Pb}$ ,  $^{226}\text{Ra}$  and  $^{137}\text{Cs}$  were counted at 2-cm intervals on a gamma spectrometer (Ortec HPGe GWL). The  $^{137}\text{Cs}$  was determined via its 662 keV photopeak, while  $^{210}\text{Pb}$  was determined via gamma emission at 46.5 keV and  $^{226}\text{Ra}$  at 295 and 352 keV  $\gamma$ -rays emitted by its daughter isotope  $^{214}\text{Pb}$ , following three weeks of storage in sealed containers to allow radioactive equilibration. Concentrations of  $^{210}\text{Pb}_{\text{ex}}$  were calculated by subtracting the  $^{226}\text{Ra}$ -supported  $^{210}\text{Pb}$  concentrations ( $^{210}\text{Pb}_{\text{sup}}$ ) from the total  $^{210}\text{Pb}$  activities ( $^{210}\text{Pb}_{\text{total}}$ ) (Appleby, 2001).

Particle size spectra of sediments were measured at 1-cm intervals using a Malvern automated laser optical particle-size analyser (Mastersizer-2000) after the removal of carbonates by 10% HCl and organic matter by 30%  $\text{H}_2\text{O}_2$  with sodium hexametaphosphate as a dispersing agent. The measurement error was within 5%. Clay (<4  $\mu\text{m}$ ) content and median grain size were shown in this study. SCP in the sediments was extracted at 2-cm intervals using  $\text{HNO}_3$ , HF and HCl according to Rose (1994). Particles larger than 8  $\mu\text{m}$  were identified and counted using an Olympus CX21

microscope at 400× magnification (Rose, 2008). SCP concentrations are expressed as grains per gram dry mass of sediment (grains g<sup>-1</sup>). SCPs in LH were not analysed.

## 2.4 Numeric models

Because the appropriate choice of the calculation model is not known *a priori*, the CIC, CFCS, CRS, <sup>137</sup>Cs-corrected CRS and SCP-corrected CRS models were chosen to calculate chronologies and sedimentation rates (Appleby, 2001; Sanchez-Cabeza and Ruiz-Fernández, 2012).

The CIC model assumes that sediments have a constant initial <sup>210</sup>Pb concentration regardless of accumulation rate (Shukla and Joshi, 1989). The supply of <sup>210</sup>Pb to lake sediment must vary directly in proportion to the sedimentation rate. Under such a scenario, the sediment age  $t$  at a depth  $x$  can be calculated using the formula

$$C(x) = C(0)e^{-\lambda t} \quad (1)$$

where  $\lambda$  is the <sup>210</sup>Pb radioactive decay constant (0.03114 yr<sup>-1</sup>), and  $C(x)$  and  $C(0)$  are the <sup>210</sup>Pb<sub>ex</sub> activity at a depth  $x$  and at the surface of the core, respectively.

The CFCS model assumes that both <sup>210</sup>Pb flux and sedimentation rate are constant (Krishnaswamy et al., 1971). The <sup>210</sup>Pb<sub>ex</sub> activity versus depth relation is closely approximated by an exponential relation, in which case a plot of the logarithm of the <sup>210</sup>Pb<sub>ex</sub> against cumulative mass depth will be closely approximated by a straight line. The mean sedimentation rate can be calculated from the slope of the regression line. When the <sup>210</sup>Pb<sub>ex</sub> activities are plotted against the cumulative mass depth, the resultant least squares best fit slope is used to calculate the mass accumulation rate ( $\omega$  in g cm<sup>-2</sup> yr<sup>-1</sup>):

$$\omega = -\lambda/\text{slope} \quad (2)$$

The cumulative mass depth  $M(x)$  is calculated using the formula

$$M(x) = \int_0^x \rho(\xi) d\xi \quad (3)$$

where  $\rho(\xi)$  is the dry bulk density at depth  $\xi$ .

Using the CFCS model, the sediment age  $t$  at a depth  $x$  can be calculated using the equation:

$$t = \frac{M(x)}{\omega} \quad (4)$$

Where sedimentation rates have varied, the plot of  $^{210}\text{Pb}_{\text{ex}}$  versus depth will deviate significantly from an exponential relation and one of the more complex models must be used. The CRS model assumes that in these cases the flux of  $^{210}\text{Pb}_{\text{ex}}$  to the sediment surface remains constant regardless of any such variations (Appleby and Oldfield, 1978). This method relies on the ratio of the cumulative residual  $^{210}\text{Pb}_{\text{ex}}$  beneath a given depth to the total  $^{210}\text{Pb}_{\text{ex}}$  activity in the sediment column. It is therefore imperative that the entire  $^{210}\text{Pb}$  inventory of a core is measured or estimated as accurately as possible.

The inventory is calculated as

$$A(x) = \int_{M(x)}^{\infty} C(m) dm \quad (5)$$

$$A(0) = \int_0^{\infty} C(m) dm \quad (6)$$

where  $C(m)$  is the mass specific  $^{210}\text{Pb}_{\text{ex}}$  concentration at mass depth  $m$ , and  $A(x)$  is the  $^{210}\text{Pb}_{\text{ex}}$  inventory beneath a given depth  $x$ .  $A(0)$  is the total  $^{210}\text{Pb}_{\text{ex}}$  activity in the sediment column. The sediment age at a depth  $x$  can be calculated using the formula

$$t = \frac{1}{\lambda} \ln \left( \frac{A(0)}{A(x)} \right) \quad (7)$$

A variety of causes such as flood events and land-use change within floodplain may cause variations in the initial  $^{210}\text{Pb}_{\text{ex}}$  concentration, probably resulting in erroneous dates in the models mentioned above. Where there are discrepancies, changes in the  $^{210}\text{Pb}$  supply rate can be calculated using independent dates by chronostratigraphic markers (Appleby, 2001). If  $x_1$  is the depth of one reference point (e.g. the  $^{137}\text{Cs}$  fallout

peak and the start of rapid increase in the SCP profile) in the core with known age  $t_1$ , the mean  $^{210}\text{Pb}$  flux ( $P$ ) above the reference point is

$$P = \frac{\lambda \Delta A}{1 - e^{-\lambda t_1}} \quad (8)$$

where  $\Delta A$  is the  $^{210}\text{Pb}$  inventory above the depth  $x_1$ .

Corrected  $^{210}\text{Pb}$  dates and sedimentation rates for intermediate depths can be derived using chronostratigraphic markers by applying the principles of the CRS model with the relevant  $^{210}\text{Pb}$  flux. The sediment age at a depth  $x$  above the depth  $x_1$  is determined by solving the equation

$$\frac{P}{\lambda} e^{-\lambda t} = \frac{P}{\lambda} e^{-\lambda t_1} + \Delta A(x_1, x) \quad (9)$$

where  $\Delta A(x_1, x)$  is the  $^{210}\text{Pb}$  inventory between  $x_1$  and  $x$ . For example, using  $^{137}\text{Cs}$  activities as independent chronostratigraphic markers, the presence of a subsurface maximum in the  $^{137}\text{Cs}$  profile will in most cases identify the 1963 depth ( $x_1$ ).

The date beneath the given depth  $x_1$  can be calculated using the formula

$$T_x = T_1 - \lambda^{-1} \ln(A_{x_1} A_x^{-1}) \quad (10)$$

where  $T_1$  and  $A_{x_1}$  are the chronostratigraphic date at the depth  $x_1$  and the  $^{210}\text{Pb}_{\text{ex}}$  inventory beneath the given depth  $x_1$ , respectively.

## 2.5 Historical document collections

The studied eight lakes are located in Hunan, Hubei and Jiangxi provinces, respectively (Table 1). In order to validate changes in sedimentation rates of the studied lakes, continuous annual data for suspended sediment concentration (1956-2013) at Datong Station and total capacity of reservoirs in the Yangtze basin (1954-2003) were sourced from Dai et al. (2016). Discontinuous data for arable land area (1887-2008) and lake area (1875-2008) in Hunan, Hubei and Jiangxi provinces were collected from published documents (Cao et al., 2014; Cui et al., 2013). In order to provide context for

the SCP profiles, continuous annual data for coal consumption in Hunan, Hubei and Jiangxi provinces (1949-2009) were collected from compendium of statistics for China's coal industry (China National Coal Association, 2011). The sequential *t*-test analysis of regime-shifts (STARS) algorithm was used to determine the shifts with the respective mean values and to evaluate the confidence levels for coal consumption data in each province and SCP concentration data of each core (Rodionov, 2004), using a cut-off length of 10 points ( $p < 0.05$ ).

### **3. Results**

#### **3.1 Particle size**

Lake sediments in the study area are characterized by fine particles, with mean percentage of clay accounting for 40-60% in the eight cores (Fig. 2). Median grain size in lake sediments mainly ranged from 2 to 8  $\mu\text{m}$ , except in the upper strata of HH and PY. There were some differences in the particle size spectra among the eight cores. Median grain size in DT and FT showed fluctuating trends in the lower strata, and subsequently increased in the upper 10 cm of sediment. In HH, LH and WH, median grain size increased broadly from the lower to upper section. Median grain size in SH and YX fluctuated below 20 cm and then remained relatively stable in the upper 20 cm. Median grain size in PY increased generally in the lower strata, followed by a decrease in the upper 10 cm of sediment.

#### **3.2 Caesium-137 profiles**

The distributions of  $^{137}\text{Cs}$  in the eight sediment cores are presented in Fig. 3. To facilitate comparison of the data from the eight cores, mass depth ( $\text{g cm}^{-2}$ ) was used in order to reduce the influence of different rates of compaction. The  $^{137}\text{Cs}$  activities in 6

out of the 8 sediment cores generally increased from 0 Bq kg<sup>-1</sup> in the bottom layers to the peak values (ranging from 11 to 28 Bq kg<sup>-1</sup>), followed by declining trends (Fig. 3). The generally low activities (< 30 Bq kg<sup>-1</sup>) of <sup>137</sup>Cs probably resulted from relatively greater losses from the lakes via the outflow, due to the high solubility of <sup>137</sup>Cs. <sup>137</sup>Cs was above 4 Bq kg<sup>-1</sup> at the bottom of the profile in DT, indicating that shorter timespan of sedimentary material was recovered (Fig. 3a). The <sup>137</sup>Cs activities in PY were very low and below the detection limit (Fig. 3h), probably resulting from its fast hydraulic flushing of the lake (mean retention time of ca. 52 days; Wang and Dou, 1998). Most of the cores have one well-defined <sup>137</sup>Cs peak, corresponding to the peak fallout of <sup>137</sup>Cs in 1963 AD from atmospheric nuclear weapons testing. The total <sup>137</sup>Cs inventory was 3665 Bq m<sup>-2</sup> in DT, 597 Bq m<sup>-2</sup> in HH, 1323 Bq m<sup>-2</sup> in LH, 1309 Bq m<sup>-2</sup> in FT, 897 Bq m<sup>-2</sup> in SH, 1625 Bq m<sup>-2</sup> in YX and 714 Bq m<sup>-2</sup> in WH, respectively (Table 2). Based on the modified <sup>137</sup>Cs reference inventory model for China, Zhang et al. (2015) estimated that the range of <sup>137</sup>Cs reference inventory in central China is between 1292 and 2119 Bq m<sup>-2</sup>. The total <sup>137</sup>Cs inventory for LH, FT and YX was consistent with the reference values. The <sup>137</sup>Cs inventory of DT was much higher than the reference values, indicating enhanced deposition due to sediment focusing or catchment-derived <sup>137</sup>Cs inputs. In contrast, the total <sup>137</sup>Cs inventory for HH, SH and WH was lower than the reference values, probably due to the removal of <sup>137</sup>Cs via lake outflows.

### 3.3 Lead-210 profiles

Supported <sup>226</sup>Ra concentrations were virtually constant in each core (Fig. 4). <sup>210</sup>Pb<sub>total</sub> activity reached a radioactive equilibrium with <sup>226</sup>Ra activity at the bottom layer of HH, LH and SH cores, but not at that of DT and PY cores (Fig. 4). In FT, YX and WH, <sup>210</sup>Pb<sub>total</sub> activity reached an equilibrium value that was greater than <sup>226</sup>Ra activity (Fig.

4), probably due to an efficiency calibration error with the gamma spectrometers. In order to remove the discrepancy, a correction value was calculated by subtracting the mean supported  $^{226}\text{Ra}$  activity from the mean asymptotic activity of  $^{210}\text{Pb}_{\text{total}}$  at the bottom samples of FT, YX and WH, respectively. The correction value was subtracted from the original  $^{210}\text{Pb}_{\text{ex}}$  activity at each level to obtain the corrected  $^{210}\text{Pb}_{\text{ex}}$  activities in FT, YX and WH, respectively (Fig. 5). The activities of  $^{210}\text{Pb}_{\text{ex}}$  in the surface sediments varied considerably, from 191 to 515  $\text{Bq kg}^{-1}$ , almost by a factor of 2 (Table 2). The maximum concentration was found in a subsurface layer in 7 out of the 8 sediment cores (376  $\text{Bq kg}^{-1}$  at 2.5 cm in DT; 333  $\text{Bq kg}^{-1}$  at 1.5 cm in LH; 529  $\text{Bq kg}^{-1}$  at 2.5 cm in FT; 382  $\text{Bq kg}^{-1}$  at 1.5 cm in SH; 356  $\text{Bq kg}^{-1}$  at 9.5 cm in YX; 287  $\text{Bq kg}^{-1}$  at 2.5 cm in WH; 221  $\text{Bq kg}^{-1}$  at 1.5 cm in PY), except HH (462  $\text{Bq kg}^{-1}$  at the surface).  $^{210}\text{Pb}_{\text{ex}}$  activities generally declined exponentially with mass depth ( $R^2 > 0.55$ ). The mean annual flux of  $^{210}\text{Pb}_{\text{ex}}$  was 2920  $\text{Bq m}^{-2} \text{yr}^{-1}$  in DT, 965  $\text{Bq m}^{-2} \text{yr}^{-1}$  in HH, 880  $\text{Bq m}^{-2} \text{yr}^{-1}$  in LH, 947  $\text{Bq m}^{-2} \text{yr}^{-1}$  in FT, 781  $\text{Bq m}^{-2} \text{yr}^{-1}$  in SH, 1132  $\text{Bq m}^{-2} \text{yr}^{-1}$  in YX, 730  $\text{Bq m}^{-2} \text{yr}^{-1}$  in WH and 1754  $\text{Bq m}^{-2} \text{yr}^{-1}$  in PY, respectively. The mean annual fluxes of  $^{210}\text{Pb}_{\text{ex}}$  were 2-7.3 times higher than the atmospheric deposition flux at Shanghai City (the delta of the Yangtze River) of  $385 \pm 62 \text{ Bq m}^{-2} \text{yr}^{-1}$  (Du et al., 2015). The fluxes in HH, LH, FT, SH and WH were similar to the value of ca.  $920 \text{ Bq m}^{-2} \text{yr}^{-1}$  for Taihu Lake, located in the lower Yangtze floodplain (Xue and Yao, 2011).

Generally, fine particles with greater specific surface areas typically contain higher radionuclide concentrations, and so clay particles are important in the transport and deposition of  $^{210}\text{Pb}$ , as suggested by significantly positive correlations between clay and  $^{210}\text{Pb}_{\text{ex}}$  observed in previous studies (Liu et al., 2009; Sun et al., 2017). In contrast, the clay component and  $^{210}\text{Pb}_{\text{ex}}$  were significantly negatively correlated in most of our cores ( $r < -0.32$ ,  $p < 0.05$ ), or non-significantly correlated in DT and YX ( $r > -0.3$ ,  $p > 0.1$ ). It

seems that the preferential adsorption of  $^{210}\text{Pb}_{\text{ex}}$  on fine particles cannot be assumed in the studied lakes. High content of clay (40-60%) in the studied lakes indicated relatively stable hydrological conditions, which would promote the deposition of  $^{210}\text{Pb}$  in these floodplain lakes. Due to dam construction in the upstream during recent decades, erosion of the downstream riverbed has strengthened and coarse particles have been transported into the lakes (Zeng et al., 2018). As a result, clay content in the upper strata has declined and opposed the trend in  $^{210}\text{Pb}_{\text{ex}}$ .

### 3.4 SCP profiles

SCP concentration maxima in this study are similar to those observed in other Yangtze floodplain sites, such as the Jiangnan Plain (4000-15000 grains  $\text{g}^{-1}$ ; Boyle et al., 1999), Taihu Lake (600-9000 grains  $\text{g}^{-1}$ ; Cao et al., 2013; Rose et al., 2004), Longgan Lake (3000-4000 grains  $\text{g}^{-1}$ ; Wu et al., 2005) and Sanliqi Lake (8000 grains  $\text{g}^{-1}$ ; Chen et al., 2014). The variations among the sediment cores are probably influenced by SCP emission from the local industries (Boyle et al., 1999) and other site specific processes such as sediment focusing (Rose, 2001). Generally, the SCP profiles showed similar trends (Fig. 6). Low concentrations in the lower strata of the profiles were followed by rapid increases before reaching a peak. Above the peak, the SCP concentrations fluctuated around 3000-8000 grains  $\text{g}^{-1}$ , followed by a decrease to the sediment surface. Coal consumption in Hunan, Hubei and Jiangxi provinces increased slowly before reaching a peak around 1960, and then decreased and fluctuated between 1961 and 1969 (Fig. 7). For each province, coal consumption increased rapidly from 1970, except a transient slump around 2000 (Fig. 7). The trough around 2000 was still higher than the historical peak in 1960. The results of regime shift detection applied for coal consumption data are presented in Fig. 7, indicating three to four significant shifts

( $p < 0.05$ ). The first shift happened in 1970 in Hubei, in 1969 in both Jiangxi and Hunan, respectively. In the seven studied cores, low SCP concentrations in the lower strata should be consistent with a low level of coal consumption between the 1950s and 1960s. The start of the rapid increase in SCP concentrations was identified by the regime shift detection (Fig. 6), which should correspond to the major expansion in coal consumption since 1970. Hence, the date of the depth, above which the SCP concentrations started to increase rapidly, should be around 1970 (Figs. 6 and 7).

### **3.5 Chronologies and sedimentation rates**

We applied the CFCS, CIC, CRS,  $^{137}\text{Cs}$ -corrected CRS and SCP-corrected CRS models to the eight cores. Chronologies provided by alternative models differed, but the tendencies observed were similar for each core (Fig. 8 and Appendix 1). Generally, the  $^{137}\text{Cs}$ -corrected CRS model produced older ages than other models. The CFCS and CIC models generally produced younger ages for the lower sections of the cores. Ages deduced from the SCP-corrected CRS model were intermediate, in comparison with the results from the CRS and  $^{137}\text{Cs}$ -corrected CRS models. Chronologies provided by the CFCS and CRS models showed a good fit in the upper strata of HH, LH, FT and SH (Figs. 8b-e). In LH, ages calculated using different models were broadly consistent (Fig. 8c).

Sedimentation rates estimated by the CRS, SCP-corrected CRS and  $^{137}\text{Cs}$ -corrected CRS models are showed in Fig.9. As a result of the discrepancies among multiple models, we obtained different changes in sedimentation rates. Generally, the sedimentation rates (SARs) increased gradually to a maximum ( $0.5\text{-}2.5 \text{ g cm}^{-2} \text{ yr}^{-1}$ ), and then declined in each core. The timing of maximum SARs was different for alternative

models, e.g., in the 1950s using the  $^{137}\text{Cs}$ -corrected CRS model, in the 1960s based on the SCP-corrected CRS model, and in the 1970s using the CRS model.

## **4. Discussion**

### **4.1 Alternative $^{210}\text{Pb}$ dating models**

The chronologies estimated by alternative models showed significant discrepancy in the same core, as also observed in former studies (Blais et al., 1995; von Gunten et al., 2009). The CIC model resulted in large time inversions, especially for the lower part of the profiles, which is consistent with previous studies because the  $^{210}\text{Pb}$  profile is non-monotonic in these lakes (Baskaran et al., 2014; von Gunten et al., 2009). During the mid-20th century, widespread deforestation in the upstream regions and land reclamation of lake margin regions for farming have increased soil erosion and so sedimentation rates in the Yangtze floodplain lakes (Xiang et al., 2002; Xu et al., 2017).  $^{210}\text{Pb}_{\text{ex}}$  fallout can be rapidly absorbed by the clay minerals and organic matter in the surface soil and its redistribution will occur in association with erosion and sediment transport processes (Gaspar et al., 2013). Recycled  $^{210}\text{Pb}_{\text{ex}}$  fallout on catchments via surface runoff delivery and sediment focusing probably contribute to enhanced  $^{210}\text{Pb}$  supply rates in these floodplain lakes (Appleby, 2008; Tylmann et al., 2016). Since most lakes have a large catchment area/surface area ratio (Table 1), the erosional input from the watershed could contribute significant proportions of  $^{210}\text{Pb}$  inventories. Alterations in initial concentrations of  $^{210}\text{Pb}$  and sedimentation rates indicate the failure of the assumption of a constant sedimentation rate and constant initial concentration of  $^{210}\text{Pb}$  (Abril and Brunskill, 2014), and hence the CIC and CFCS models failed to yield a reliable chronology.

The CRS model allows changes in the initial concentrations and the sedimentation rates at different layers, assuming constant  $^{210}\text{Pb}_{\text{ex}}$  flux to the sediment surface (Appleby and Oldfield, 1978). Usually, the CRS model yields more realistic results than the CIC model (Appleby, 2008). In this study, the unconstrained CRS model- yielded ages were younger than the  $^{137}\text{Cs}$  and SCP chronomarkers (1963 and 1970 AD) at the corresponding horizon of each core (Fig. 8). Underestimation of sediment ages by the unconstrained CRS model was also reported in previous studies (Tylmann et al., 2016). These relatively young sediment ages probably resulted from the declining  $^{210}\text{Pb}_{\text{ex}}$  inventory in the upper strata, because the influx of sediment and recycled  $^{210}\text{Pb}_{\text{ex}}$  from the catchment decreased after reservoir construction and soil conservation measures were instated in the upper catchment after the 1970s (Dai et al., 2016; see the details in section 4.2). In the upper strata of the eight cores (above  $10 \text{ g cm}^{-2}$ ), the  $^{210}\text{Pb}_{\text{ex}}$  activities declined rapidly with depth (Fig. 5), indicating that SARs were lower in the upper strata than in the lower layers (cf. Mabit et al., 2014). In cases where there is significant discrepancy between the CRS model chronologies and the  $^{137}\text{Cs}$  and SCP chronomarkers, corrected  $^{210}\text{Pb}$  dates can be calculated by applying the CRS model in a stepwise way to different sections of the core using the chronostratigraphic dates as reference points (Appleby, 2008).

In each lake (except PY),  $^{137}\text{Cs}$  exhibited a sharp peak, suggesting that substantial mixing of the sediments had not occurred and the  $^{137}\text{Cs}$  peak can be an independent stratigraphic chronomarker. In the cores from HH, FT, SH and WH, the  $^{137}\text{Cs}$ -corrected CRS model overestimated sediment ages in the lower layers (stratigraphically below the 1963 fallout peak), in comparison with the unconstrained CRS and SCP-corrected CRS models (Fig. 8). The results might be linked to delayed delivery of  $^{137}\text{Cs}$  from the watershed. Besides direct atmospheric fallout,  $^{137}\text{Cs}$  is easily transported in dissolved

form from upstream soils into lakes by surface runoff (Putyrskaya et al., 2009), which is another important source for  $^{137}\text{Cs}$  in lake sediments (Ritchie and McHenry, 1990; Walling and He, 1997). The peak of the total  $^{137}\text{Cs}$  in the lake stratigraphies probably reached several years after the maximum atmospheric fallout, because the continuous input of  $^{137}\text{Cs}$  from the catchment into the lake, which would be exacerbated by soil erosion, dominates over radioactive decay before the peak is reached (Putyrskaya et al., 2009). Hence, the impact of  $^{137}\text{Cs}$  delivery from the watershed is likely to be important. In addition, the  $^{137}\text{Cs}$  profile can be impacted by vertical diffusion because caesium is an element susceptible to dissolution (Xiang et al., 2002; Putyrskaya et al., 2009).

Apart from the initial  $^{137}\text{Cs}$  peak, the secondary peak was not observed in the  $^{137}\text{Cs}$  profiles (Fig. 3), indicating that the chronomarker of the 1986 Chernobyl accident is not available in our studied lakes. The peak identified as the 1986 fallout was observed in some lakes of the Yangtze floodplain (e.g. Gucheng Lake; Xiang et al., 2002), but may result from sediment mixing and upward migration of caesium. The distribution of Chernobyl fallout was very uneven and mainly controlled by the path of the radioactive plume and its coincidence with rainfall (Appleby, 2001). Former studies have revealed that the 1986 Chernobyl fallout was mainly observed at sites in Europe and the western former USSR (Ritchie and McHenry, 1990). The  $^{137}\text{Cs}$  profiles of 18 lakes in East Asia and the annual  $^{137}\text{Cs}$  deposition flux for Tokyo indicate that the Chernobyl fallout is not significant in the East Asian region (Zhang et al., 2012).

SCPs are inert to changes in water and sediment chemistry (Rose, 2001), and they could not be transported in dissolved form as for  $^{137}\text{Cs}$ . However, SCPs may enter lakes with soil particles when catchment erosion occurs. After deposition SCPs show no apparent degradation and post-depositional changes in lake sediments (Rose, 1999; Rose and Appleby, 2005). Hence, whilst soil erosion processes may deliver soil-derived

SCP particles to lakes, the magnitude of changes in sediment flux was always < 10-fold, setting boundaries on the possible SCP contributions from soil erosion (Fig. 10). It is likely that a good proportion of eroded soil was old and so SCP-free. In contrast, concentrations of SCP particles increased in the order of  $10^3$ , making it unlikely that soil erosion processes could be responsible for altering the down-core patterns in SCP concentrations (Fig. 6). Since SCPs are solely anthropogenic in origin, their temporal trends are seen to be in good agreement with known historical coal consumption in Hunan, Hubei and Jiangxi provinces (Fig. 7). SCPs displayed slight decreases in surface sediments, probably due to the deployment of clean coal technologies, such as dust removal (Chang et al., 2016). In accordance with the results of previous studies in both HH and WH (Boyle et al., 1999), the start of rapid increase in SCPs in 1970 AD in this study provided a clear chronomarker for dating recent sediment. Hence, the accuracy of the chronologies for the sediment cores can be improved by validating with the SCP chronomarker in 1970 AD.

#### **4.2 Sedimentation rate changes**

Before the 1930s, most lakes were hydrologically connected with the Yangtze River, and human disturbance was weak. Under such a scenario, sedimentation rates in the Yangtze floodplain lakes were generally less than  $0.2 \text{ g cm}^{-2} \text{ yr}^{-1}$  before the 1930s (Fig. 10a), in agreement with the results of previous studies (Chen et al., 2011; Liu et al., 2012; Xiang et al., 2002; Xu et al., 2017; Xue and Yao, 2011; Yi et al., 2004; Zeng et al., 2018; Zhang et al., 2010). Between the 1930s and the 1950s, there was an extension of arable land to meet the food demands of the rising population in the Yangtze basin (Cao et al., 2014; Fig. 10b). Firstly, floodplain lakes were reclaimed for agricultural land (Cui et al., 2013; Fig. 10c). Meanwhile, intensive reclamation and deforestation

accelerated surface soil erosion, subsequently increasing sediment loading into the Yangtze floodplain lakes (Xiang et al., 2002), as suggested by rising sedimentation rates in Wushan, Shijiuhu, Guchenghu and Nanyihu lakes during this period (Zhang et al., 2010; Xue and Yao, 2011). Meanwhile, increasing summer precipitation in the early-1950s probably promoted the transport of sediment into lakes (Xue and Yao, 2011). Accordingly, sedimentation rates derived from the SCP-corrected model reached a peak in the 1960s for most of lakes in this study, such as HH, FT, SH and PY (Fig. 10a).

After 1970, the total reservoir capacity in the Yangtze basin increased rapidly (Fig. 10d), and dam trapping caused a decrease in suspended sediment in the Yangtze River (Figs. 10e). Due to the reducing influx of suspended sediment from the upper reaches, sedimentation rates in these lakes showed declining trends. For example, Zhang et al. (2010) found that sedimentation rate declined in Wushan Lake after the 1960s, resulting from the impoundment of two reservoirs in the upper catchment. Similarly, sediment trapping by several reservoirs that were built in 1958-1962 in the upper reaches, led to a reduction in sedimentation rate in Taibai Lake after the 1960s (Liu et al., 2012). Moreover, surface soil erosion and sediment discharge declined further after 1986, as a consequence of the implementation of water and soil conservation strategies in the Yangtze basin (Dai et al., 2016). Based on the SCP-corrected CRS model, sedimentation rates in the studied lakes (except DT and LH) remained relatively stable after the 1980s, with mean values ranging from 0.09 to 0.58 g cm<sup>-2</sup> yr<sup>-1</sup> (Fig. 10a). Taken together, the SCP-corrected CRS model provided results that matched historical changes in arable land and sediment discharge more closely.

DT had relatively higher sedimentation rates than other lakes (Fig. 10a), probably linked to a high influx of sediment from the catchment (Du et al., 2001). Yang et al. (2007) estimated that average annual deposition of sediment was ca. 211 Mt in the

Yangtze basin for the period 1956-2004, and more than half (~113 Mt) of sediment deposited in DT which is located in the upstream position among our lakes (Fig.1). Annual deposition of sediment in DT was high, but declined gradually after the 1950s (Yang et al., 2007), whereas SARs in DT increased gradually until 2003. It is notable that water surface area of DT decreased from ~4000 km<sup>2</sup> in the 1950s to ~2500 km<sup>2</sup> in 1998, with an average decrease rate of ~30 km<sup>2</sup> per year from 1950 (Zhao et al., 2005). Gradual increases in SARs before 2003 suggested that the effects of lake surface area shrinkage exceeded those of sediment deposition reduction in DT, at least in some parts of this large lake. In response to sediment trapping by the Three Gorges Dam impoundment, the deposition rate in DT decreased to 2 Mt/yr for the period 2003-2012 (Bulletin of Yangtze River Sediment, 2003-2015), probably accounting for a recent reduction in sedimentation rate.

## 5. Conclusions

Multiple <sup>210</sup>Pb-based dating models were tested to establish an accurate chronological framework for recent lake sediment in the Yangtze floodplain. Two independent time markers were used to validate the <sup>210</sup>Pb chronologies, including <sup>137</sup>Cs and SCP. Five models, i.e. CIC, CFCS, CRS, <sup>137</sup>Cs-corrected CRS and SCP-corrected CRS, were calculated. Compared with regional historical documents, sedimentation rates derived from the SCP-corrected CRS model matched historical changes in the Yangtze basin more closely. Due to land reclamation and deforestation, sedimentation rates generally increased between the 1930s and the 1950s, and reached a peak in the 1960s. Reservoir construction and soil conservation measures caused a decrease in sedimentation rates after the 1970s. The SCP-corrected CRS model seems to be a suitable technique for calculating chronologies and sedimentation rates in these shallow

and rapidly-flushed Yangtze floodplain lakes and other similar lacustrine systems within floodplain landscapes.

### **Acknowledgements**

We acknowledge Yang Xiangdong, Zhang Enlou, Dong Xuhui, Mao Xin, Du Chenchang, Xia Weilan, Tao Jingkui and Yao Shuchun for field and laboratory assistance. This study was supported by the National Natural Science Foundation of China (41572343, 41530753 and 41202248) and the Fundamental Research Fund for National University, China University of Geosciences (Wuhan) (G1323511656).

### **References**

- Abril, J.M., Brunskill, G.J., 2014. Evidence that excess  $^{210}\text{Pb}$  flux varies with sediment accumulation rate and implications for dating recent sediments. *J. Paleolimnol.*, 52, 121-137.
- Appleby, P.G., 2001. Chronostratigraphic Techniques in Recent Sediments. in: Last, W., Smol, J. (Eds.), *Tracking Environmental Change Using Lake Sediments*. Springer Netherlands, pp. 171-203.
- Appleby, P.G., 2008. Three decades of dating recent sediments by fallout radionuclides: a review. *Holocene*, 18, 83-93.
- Appleby, P.G., Oldfield, F., 1978. The calculation of lead-210 dates assuming a constant rate of supply of unsupported  $^{210}\text{Pb}$  to the sediment. *Catena*, 5, 1-8.
- Baskaran, M., Miller, C.J., Kumar, A., Andersen, E., Hui, J., Selegean, J.P., Creech, C.T., Barkach, J., 2015. Sediment accumulation rates and sediment dynamics using five different methods in a well-constrained impoundment: Case study from Union Lake, Michigan. *J. Gt. Lakes Res.*, 41, 607-617.

- Baskaran, M., Nix, J., Kuyper, C., Karunakara, N., 2014. Problems with the dating of sediment core using excess  $^{210}\text{Pb}$  in a freshwater system impacted by large scale watershed changes. *J. Environ. Radioact.*, 138, 355-363.
- Binford, M.W., 1990. Calculation and uncertainty analysis of  $^{210}\text{Pb}$  dates for PIRLA project lake sediment cores. *J. Paleolimnol.*, 3, 253-267.
- Blais, J.M., Kalff, J., Cornett, R.J., Evans, R.D., 1995. Evaluation of  $^{210}\text{Pb}$  dating in lake sediments using stable Pb, Ambrosia pollen, and  $^{137}\text{Cs}$ . *J. Paleolimnol.*, 13, 169-178.
- Boyle, J.F., Rose, N.L., Bennion, H., Yang, H., Appleby, P.G., 1999. Environmental impacts in the Jiangnan Plain: Evidence from lake sediments. *Water Air Soil Pollut.*, 112, 21-40.
- Bulletin of Yangtze River Sediment, 2003-2015. Press of Ministry of Water Resources of the People's Republic of China, websites: <http://www.cjh.com.cn> (in Chinese).
- Cao, X., Jin, X.B., Wang, J.S., Miao, L.J., Zhou, Y.K., 2014. Reconstruction and change analysis of cropland data of China in recent 300 years. *Acta Geogr. Sin.*, 69, 896-906.
- Cao, Y., Zhang, E., Langdon, P., Liu, E., Shen, J., 2013. Spatially different nutrient histories recorded by multiple cores and implications for management in Taihu Lake, eastern China. *Chin. Geogr. Sci.*, 23, 537-549.
- Chang, S., Zhuo J., Meng S., Qin S., Yao Q., 2016. Clean Coal Technologies in China: Current Status and Future Perspectives. *Engineering*, 2, 447-459.
- Chen, X., Li, C., McGowan, S., Yang, X., 2014. Diatom response to heavy metal pollution and nutrient enrichment in an urban lake: evidence from paleolimnology. *Int. J. Limnol.*, 50, 121-130.

- Chen, X., Yang, X., Dong, X., Liu, Q., 2011. Nutrient dynamics linked to hydrological condition and anthropogenic nutrient loading in Chaohu Lake (southeast China). *Hydrobiologia*, 661, 223-234.
- Chen, Z., Li, J., Shen, H., Wang, Z., 2001. Yangtze River of China: historical analysis of discharge variability and sediment flux. *Geomorphology*, 41, 77-91.
- China National Coal Association., 2011. Compendium of Statistics for China's Coal Industry. China Coal Industry Publishing House, Beijing
- Córdoba, F.E., Piovano, E.L., Guerra, L., Mulsow, S., Sylvestre, F., Zárata, M., 2017. Independent time markers validate  $^{210}\text{Pb}$  chronologies for two shallow Argentine lakes in Southern Pampas. *Quatern Int.*, 438, 175-186.
- Cui, L., Gao, C., Zhao, X., Ma, Q., Zhang, M., Li, W., Song, H., Wang, Y., Li, S., Zhang, Y., 2013. Dynamics of the lakes in the middle and lower reaches of the Yangtze River basin, China, since late nineteenth century. *Environ. Monit. Assess.*, 185, 4005-4018.
- Dai, Z., Fagherazzi, S., Mei, X., Gao, J., 2016. Decline in suspended sediment concentration delivered by the Changjiang (Yangtze) River into the East China Sea between 1956 and 2013. *Geomorphology*, 268, 123-132.
- Du, J., Du, J., Baskaran, M., Bi, Q., Huang, D., Jiang, Y., 2015. Temporal variations of atmospheric depositional fluxes of  $^7\text{Be}$  and  $^{210}\text{Pb}$  over 8 years (2006–2013) at Shanghai, China, and synthesis of global fallout data. *J. Geophys. Res.-Atmos.*, 120, 4323-4339.
- Du, Y., Cai, S.M., Zhang, X.Y., Zhao, Y., 2001. Interpretation of the environmental change of Dongting Lake, middle reach of Yangtze River, China, by Pb-210 measurement and satellite image analysis. *Geomorphology*, 41, 171-181.

- Gaspar, L., Navas, A., Walling, D.E., Machín, J., Gómez Arozamena, J., 2013. Using  $^{137}\text{Cs}$  and  $^{210}\text{Pb}_{\text{ex}}$  to assess soil redistribution on slopes at different temporal scales. *Catena*, 102, 46-54.
- Jweda, J., Baskaran, M., 2011. Interconnected riverine–lacustrine systems as sedimentary repositories: Case study in southeast Michigan using  $^{210}\text{Pb}$  and  $^{137}\text{Cs}$ -based sediment accumulation and mixing models. *J. Great Lakes Res.*, 37, 432-446.
- Krishnaswamy, S., Lal, D., Martin, J.M., Meybeck, M., 1971. Geochronology of lake sediments. *Earth Planet. Sci. Lett.*, 11, 407-414.
- Lan, B., Zhang, D., Yang, Y., 2018. Lacustrine sediment chronology defined by  $^{137}\text{Cs}$ ,  $^{210}\text{Pb}$  and  $^{14}\text{C}$  and the hydrological evolution of Lake Ailike during 1901–2013, northern Xinjiang, China. *Catena*, 161, 104-112.
- Liu, E., Xue, B., Yang, X., Wu, Y., Xia, W., 2009.  $^{137}\text{Cs}$  and  $^{210}\text{Pb}$  chronology for modern lake sediment: a case study of Chaohu Lake and Taibai Lake. *Mar. Geol. Quatern. Geol.*, 29, 89-94.
- Liu, Q., Yang, X., Anderson, N.J., Liu, E., Dong, X., 2012. Diatom ecological response to altered hydrological forcing of a shallow lake on the Yangtze floodplain, SE China. *Ecohydrology*, 5, 316-325.
- Mabit, L., Benmansour, M., Abril, J.M., Walling, D.E., Meusbürger, K., Iurian, A.R., Bernard, C., Tarján, S., Owens, P.N., Blake, W.H., Alewell, C., 2014. Fallout  $^{210}\text{Pb}$  as a soil and sediment tracer in catchment sediment budget investigations: A review. *Earth-Sci. Rev.*, 138, 335-351.
- Oldfield, F., Appleby, P.G., Battarbee, R.W., 1978. Alternative  $^{210}\text{Pb}$  dating: results from the New Guinea Highlands and Lough Erne. *Nature*, 271, 339.

- Olson, D.M., Dinerstein, E., 1998. The Global 200: A Representation Approach to Conserving the Earth's Most Biologically Valuable Ecoregions. *Conserv. Biol.*, 12, 502-515.
- Pennington, W., Cambray R, S., Eakins J, D., Harkness D, D., 1976. Radionuclide dating of the recent sediments of Blelham Tarn. *Freshw. Biol.*, 6, 317-331.
- Putyrskaya, V., Klemt, E., Röllin, S., 2009. Migration of <sup>137</sup>Cs in tributaries, lake water and sediment of Lago Maggiore (Italy, Switzerland) - analysis and comparison with Lago di Lugano and other lakes. *J. Environ. Radioact.*, 100, 35-48.
- Ritchie, J.C., McHenry, J.R., 1990. Application of radioactive fallout cesium-137 for measuring soil-erosion and sediment accumulation rates and patterns - a review. *J. Environ. Qual.*, 19, 215-233.
- Robbins, J.A., Edgington, D.N., 1975. Determination of recent sedimentation rates in Lake Michigan using Pb-210 and Cs-137. *Geochim. Cosmochim. Ac.*, 39, 285-304.
- Rodionov, S.N., 2004. A sequential algorithm for testing climate regime shifts. *Geophys. Res. Lett.*, 31, L09204
- Rose, N.L., 1994. A note on further refinements to a procedure for the extraction of carbonaceous fly-ash particles from sediments. *J. Paleolimn.*, 11, 201-204.
- Rose, N.L., 2001. Fly-Ash Particles. In: Last, W.M., Smol, J.P. (Eds.), *Tracking Environmental Change Using Lake Sediments: Physical and Geochemical Methods*. Springer Netherlands, Dordrecht, pp. 319-349.
- Rose, N.L., 2008. Quality control in the analysis of lake sediments for spheroidal carbonaceous particles. *Limnol. Oceanogr. Meth.*, 6, 172-179.
- Rose, N.L., Appleby, P.G., 2005. Regional Applications of Lake Sediment Dating by Spheroidal Carbonaceous Particle Analysis I: United Kingdom. *J. Paleolimnol.*, 34, 349-361.

- Rose, N.L., Boyle, J.F., Du, Y., Yi, C., Dai, X., Appleby, P.G., Bennion, H., Cai S., Yu, L., 2004. Sedimentary evidence for changes in the pollution status of Taihu in the Jiangsu region of eastern China. *J. Paleolimnol.*, 32, 41-51.
- Rose, N.L., Harlock, S., Appleby, P.G., 1999. The Spatial and Temporal Distributions of Spheroidal Carbonaceous Fly-Ash Particles (SCP) in the Sediment Records of European Mountain Lakes. *Water Air Soil Pollut.*, 113, 1-32.
- Sanchez-Cabeza, J.A., Ruiz-Fernández, A.C., 2012.  $^{210}\text{Pb}$  sediment radiochronology: An integrated formulation and classification of dating models. *Geochim. Cosmochim. Ac.*, 82, 183-200.
- Shukla, B.S., Joshi, S.R., 1989. An evaluation of the CIC model of  $^{210}\text{Pb}$  dating of sediments. *Environ. Geol. Water Sci.*, 14, 73-76.
- Smith, J.N., 2001. Why should we believe  $^{210}\text{Pb}$  sediment geochronologies? *J. Environ. Radioact.*, 55, 121-123.
- Sun, X., Fan, D., Tian, Y., Zheng, S., 2017. Normalization of excess  $^{210}\text{Pb}$  with grain size in the sediment cores from the Yangtze River Estuary and adjacent areas: Implications for sedimentary processes. *Holocene*, 28, 545-557.
- Tylmann, W., Bonk, A., Goslar, T., Wulf, S., Grosjean, M., 2016. Calibrating  $^{210}\text{Pb}$  dating results with varve chronology and independent chronostratigraphic markers: Problems and implications. *Quat. Geochronol.*, 32, 1-10.
- Tylmann, W., Enters, D., Kinder, M., Moska, P., Ohlendorf, C., Poręba, G., Zolitschka, B., 2013. Multiple dating of varved sediments from Lake Łazduny, northern Poland: Toward an improved chronology for the last 150 years. *Quat. Geochronol.*, 15, 98-107.

- von Gunten, L., Grosjean, M., Beer, J., Grob, P., Morales, A., Urrutia, R., 2009. Age modeling of young non-varved lake sediments: methods and limits. Examples from two lakes in Central Chile. *J. Paleolimnol.*, 42, 401-412.
- Walling, D.E., He, Q., 1997. Use of fallout  $^{137}\text{Cs}$  in investigations of overbank sediment deposition on river floodplains. *Catena*, 29, 263-282.
- Wang, S., Dou, H., 1998. Lakes in China. Science Press, Beijing.
- Wu, Y., Wang, S., Xia, W., Liu, J., 2005. Dating recent lake sediments using spheroidal carbonaceous particle (SCP). *Chin. Sci. Bull.*, 50, 1016-1020.
- Xiang, L., Lu, X.X., Higgitt, D.L., Wang, S.M., 2002. Recent lake sedimentation in the middle and lower Yangtze basin inferred from  $^{137}\text{Cs}$  and  $^{210}\text{Pb}$  measurements. *J. Asian Earth Sci.*, 21, 77-86.
- Xie, C., Huang, X., Mu, H., Yin, W., 2017. Impacts of Land-Use Changes on the Lakes across the Yangtze Floodplain in China. *Environ. Sci. Technol.*, 51, 3669-3677.
- Xu, M., Dong, X., Yang, X., Chen, X., Zhang, Q., Liu, Q., Wang, R., Yao, M., Davidson, A.T., Jeppesen, E., 2017. Recent Sedimentation Rates of Shallow Lakes in the Middle and Lower Reaches of the Yangtze River: Patterns, Controlling Factors and Implications for Lake Management. *Water*, 9.
- Xue, B., Yao, S., 2011. Recent sedimentation rates in lakes in lower Yangtze River basin. *Quatern Int.*, 244, 248-253.
- Yang, S.L., Zhang, J., Dai, S.B., Li, M., Xu, X.J., 2007. Effect of deposition and erosion within the main river channel and large lakes on sediment delivery to the estuary of the Yangtze River. *J. Geophys. Res.-Earth Surf.*, 112.
- Yi, C.L., Appleby, P.G., Boyle, J.F., Rose, N.L., Dai, X.R., Xie, P., 2004. The sedimentary record of a significant flooding event in Lake Taihu on the Yangtze Delta, China. *J. Coast. Res.*, 89-100.

- Zeng, L., McGowan, S., Cao, Y., Chen, X., 2018. Effects of dam construction and increasing pollutants on the ecohydrological evolution of a shallow freshwater lake in the Yangtze floodplain. *Sci. Total Environ.*, 621, 219-227.
- Zhang, E.L., Jones R., Langdon P., Yang X., Shen J., 2010. A 150-year record of recent changes in human activity and eutrophication of Lake Wushan from the middle reach of the Yangtze River, China. *J. Limnol.*, 69, 235-241.
- Zhang, W., Pan, S., Zhang, K., Cao, L., Zhao, J., 2015. Study of the Cesium-137 Reference Inventory in the Mainland of China. *Acta Geogr. Sin.*, 9, 011.
- Zhang, X., Long, Y., Wen, A., He, X., 2012. Discussion on applying  $^{137}\text{Cs}$  and  $^{210}\text{Pb}_{\text{ex}}$  for lake sediment dating in China. *Quatern. Sci.*, 32, 430-440.
- Zhao, S.Q., Fang, J.Y., Miao, S.L., Gu, B., Tao, S., Peng, C.H., Tang, Z.Y., 2005. The 7-decade degradation of a large freshwater lake in central Yangtze river, China. *Environ. Sci. Technol.*, 39, 431-436.

## Figure captions

Figure 1 Location of the study area in China (labelled with a red rectangle; A) and the middle Yangtze reaches with the eight studied lakes shown (B).

Figure 2 Clay content and median grain size of the eight studied cores arranged by position along the Yangtze River (upstream to downstream), including (a) DT, (b) HH, (c) LH, (d) FT, (e) SH, (f) YX, (g) WH and (h) PY.

Figure 3  $^{137}\text{Cs}$  activities versus mass depth in the eight sediment cores.

Figure 4  $^{226}\text{Ra}$  and the total  $^{210}\text{Pb}$  ( $^{210}\text{Pb}_{\text{total}}$ ) activities versus mass depth in the sediment cores.

Figure 5 Unsupported  $^{210}\text{Pb}$  ( $^{210}\text{Pb}_{\text{ex}}$ ) activities versus mass depth in the sediment cores.

Figure 6 SCP concentrations versus mass depth in the sediment cores. The thick grey line depicts the changes in mean identified by the STARS algorithm.

Figure 7 Historical coal consumption Hubei (a), Jiangxi (b) and Hunan (c) provinces. Data sourced from China National Coal Association (2011). The thick grey line depicts the changes in mean identified by the STARS algorithm.

Figure 8 Comparison of dating results derived from alternative  $^{210}\text{Pb}$  models in the sediment cores.

Figure 9 Comparison of sedimentation rates derived from the CRS,  $^{137}\text{Cs}$ -corrected CRS and SCPs-corrected CRS models in the sediment cores.

Figure 10 A comparison between (a) sedimentation rates derived from the SCPs-corrected CRS model and historical documents of the middle Yangtze reaches, including (b) total arable land area in Hunan, Hubei and Jiangxi provinces in the middle Yangtze reaches gathered from Cao et al. (2014), (c) total lake surface area of Hunan, Hubei and Jiangxi provinces sourced from Cui et al. (2013), (d) total capacity of

reservoirs in the Yangtze basin collated from Dai et al. (2016) and (e) suspended sediment concentration (SSC) at Datong Station sourced from Dai et al. (2016).



Table 1 Sampling locations and detailed information of the eight studied lakes. Most of the data is sourced from Wang and Dou (1998).

Lake	Sampling site		Sampling date	Location	Water depth (m)	Core length(cm)	Lake area (km <sup>2</sup> )	Catchment area (km <sup>2</sup> )	Dam established
	Latitude N	Longitude E							
Dongting	29°19'46.02"	112°57'36.60"	2013	Hunan	6.4	72	2500	257000	-
Honghu	29°49'10.21"	113°19'36.11"	2015	Hubei	1.9	87	344	8265	1955
Futou	30°03'16.96"	114°12'24.67"	2014	Hubei	2.9	87	115	1238	1935,1973
Luhu	30°14'24.99"	114°11'24.34"	2016	Hubei	2.7	101	40	463	1935,1967
Shahu	30°34'12.18"	114°20'11.30"	2011	Hubei	2	66	3	-	-
Yanxi	30°34'18.08"	114°28'42.49"	2011	Hubei	3.5	87	12	67	1955,1965
Wanghu	29°52'19.05"	115°18'38.41"	2016	Hubei	3.6	99	42	5310	1967
Poyang	29°10'8.75"	116°04'39.73"	2016	Jiangxi	5.1	61	2933	162000	-

Table 2 Radiometric inventories of the eight sediment cores.

Lake	Unsupported $^{210}\text{Pb}$			$^{137}\text{Cs}$ inventory Bq m <sup>-2</sup>
	Surface activity Bq kg <sup>-1</sup>	Inventory Bq m <sup>-2</sup>	Flux Bq m <sup>-2</sup> yr <sup>-1</sup>	
Dongting	333	93778	2920	3665
Honghu	462	30986	965	597
Futou	515	30426	947	1309
Luhu	324	28250	880	1323
Shahu	287	25090	781	897
Yanxi	247	36367	1132	1625
Wanghu	276	23439	730	714
Poyang	191	56324	1754	-

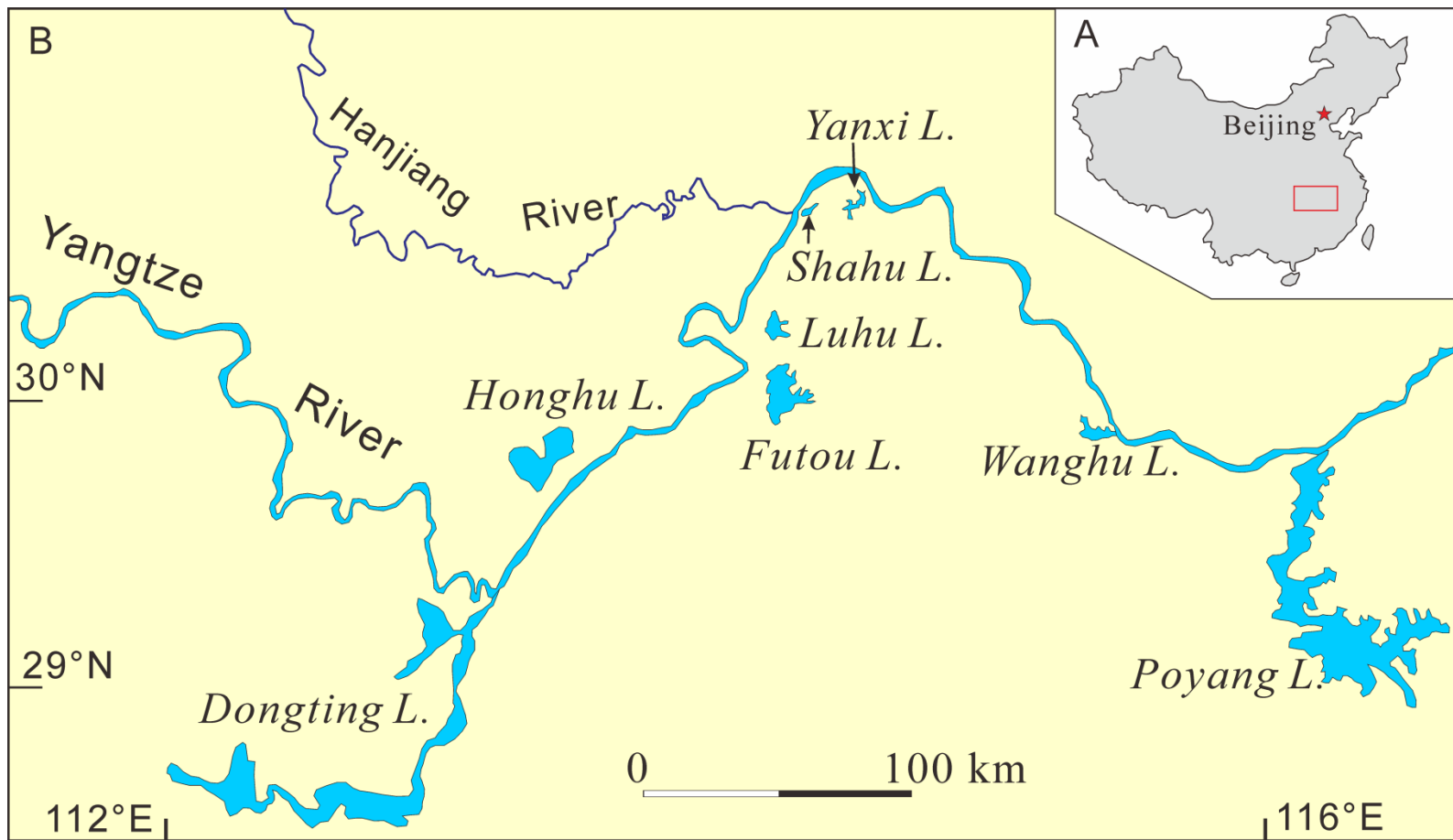


Figure 1

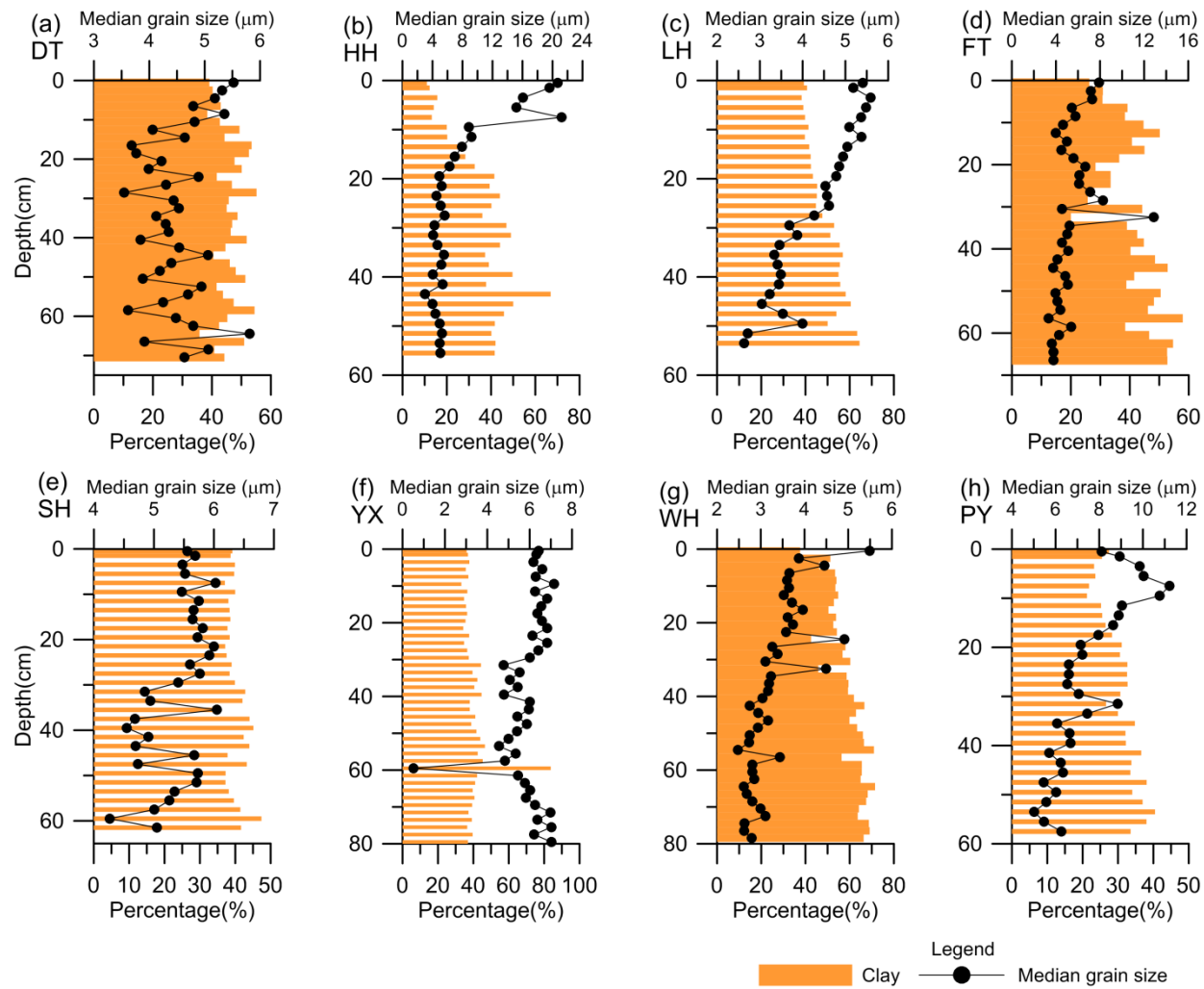


Figure 2

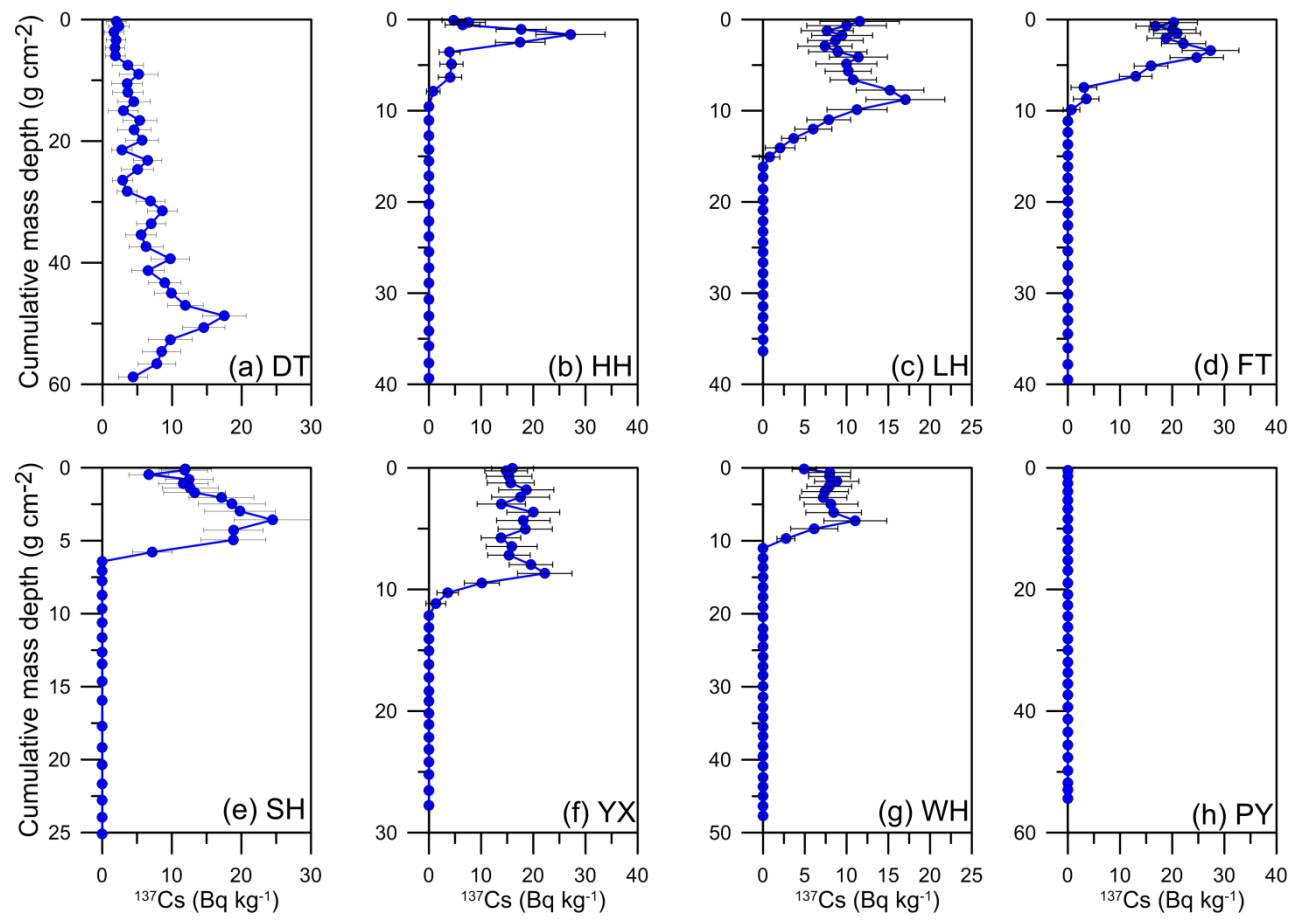


Figure 3

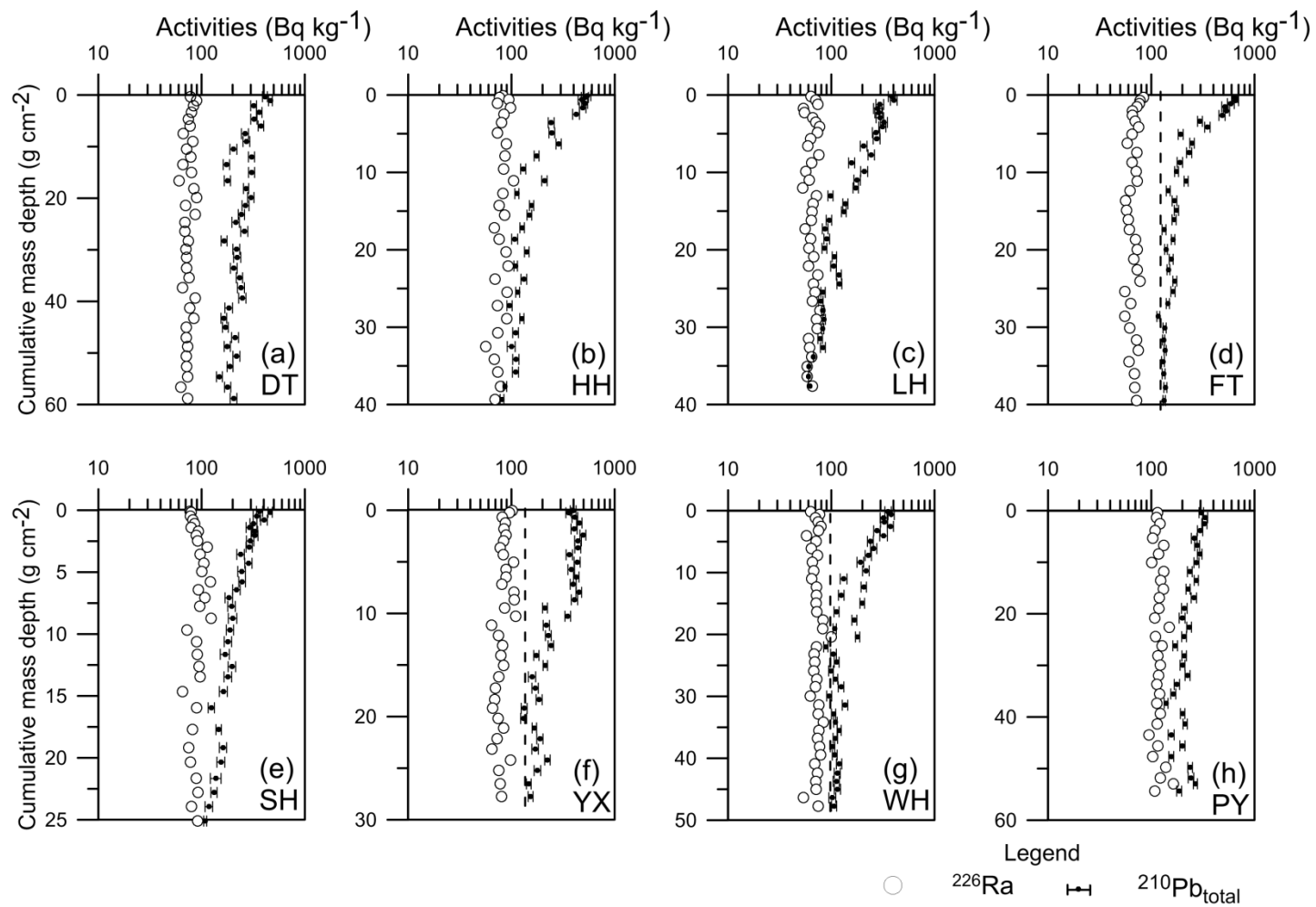


Figure 4

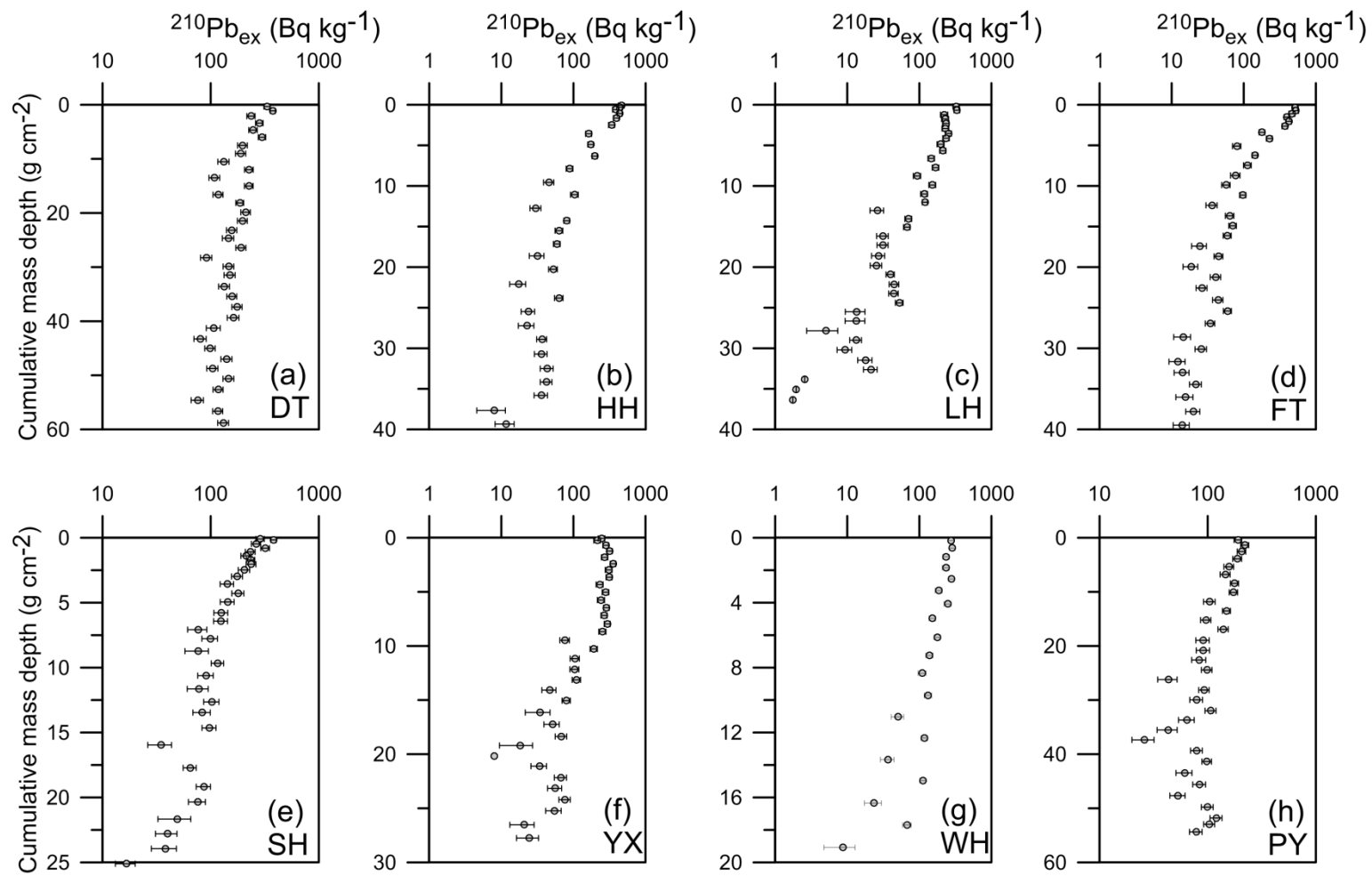


Figure 5

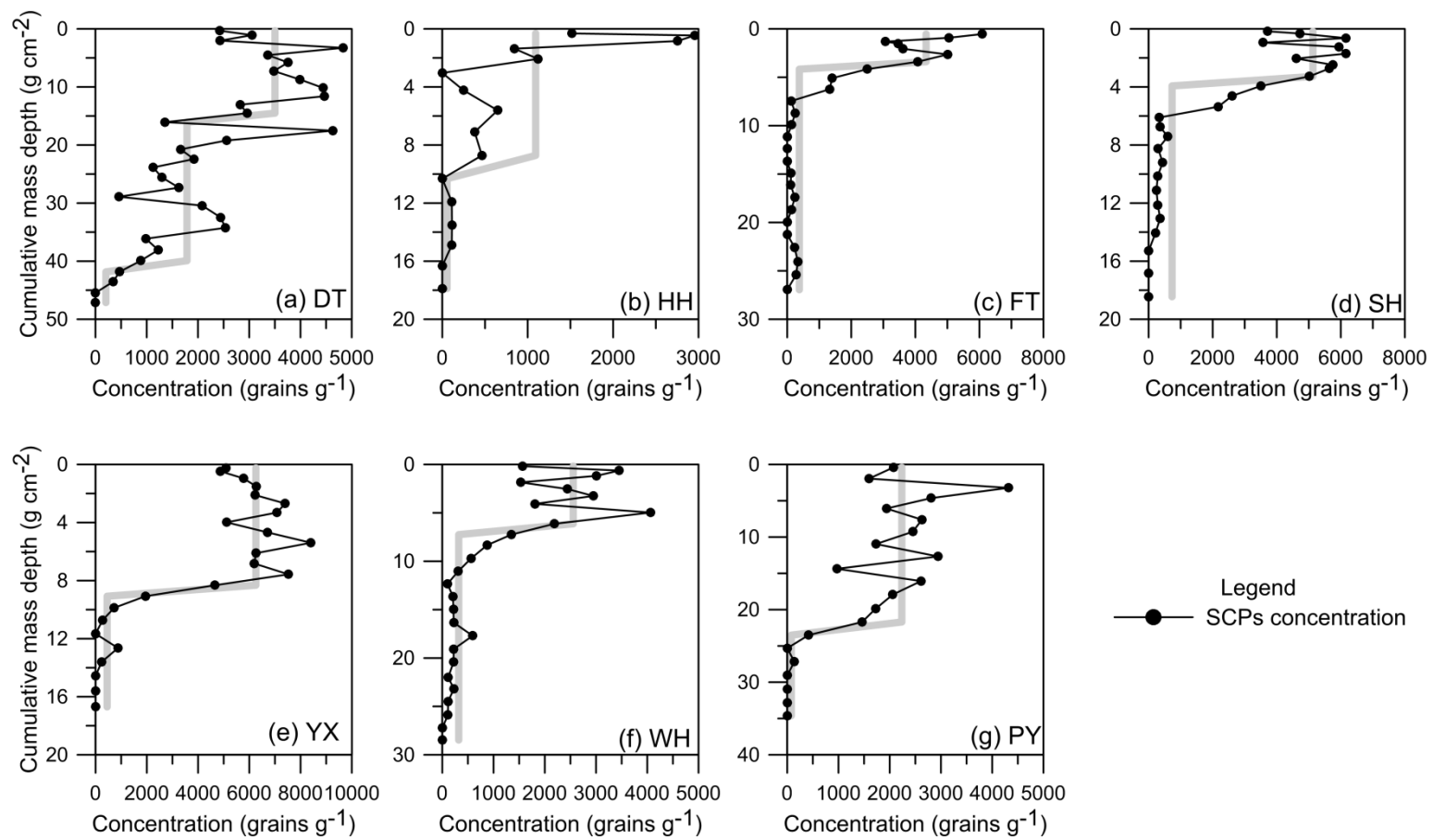


Figure 6

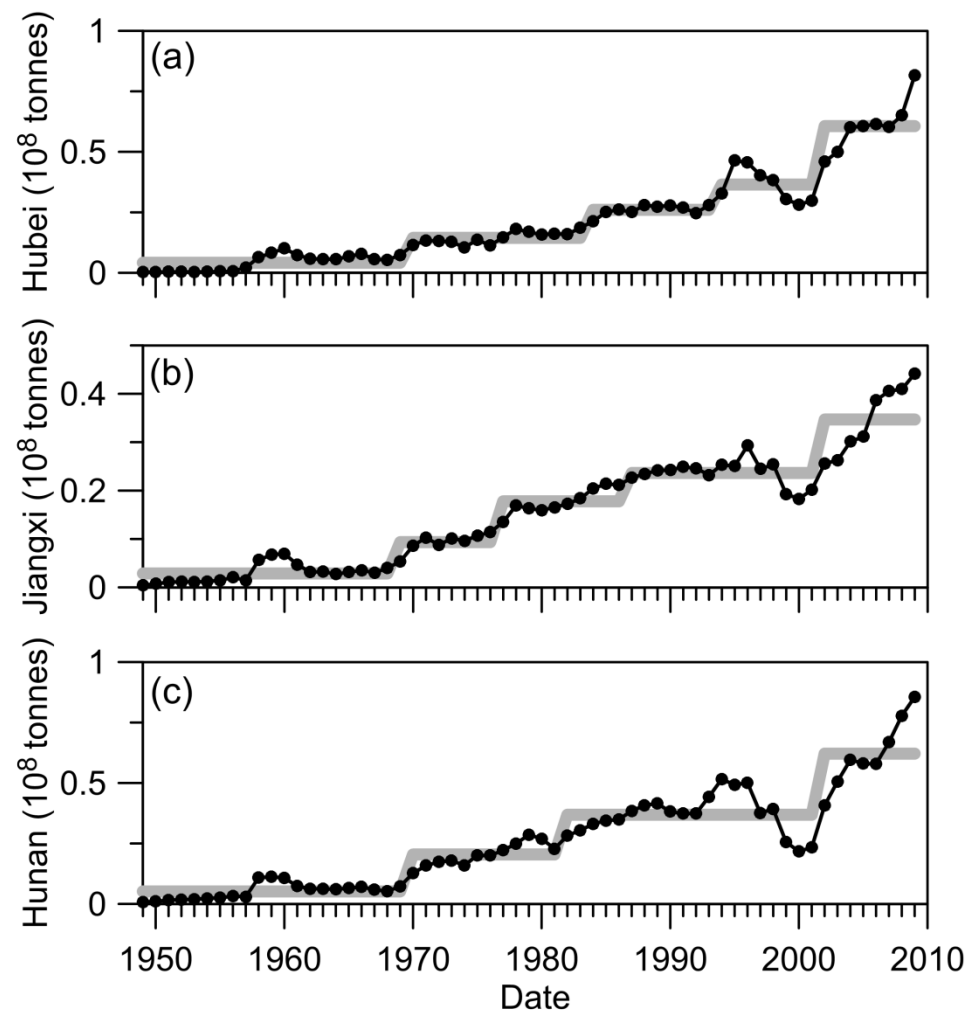


Figure 7

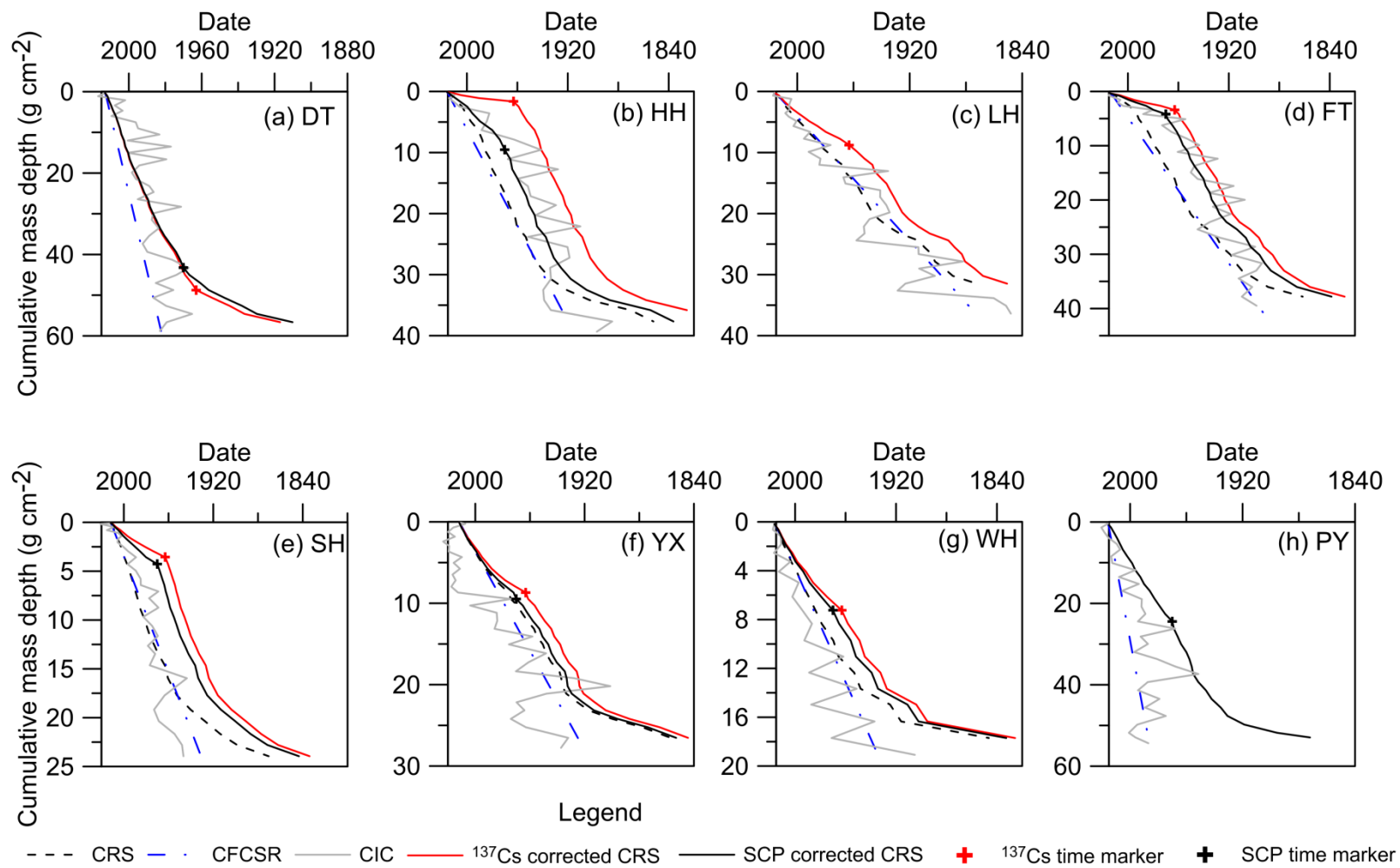


Figure 8

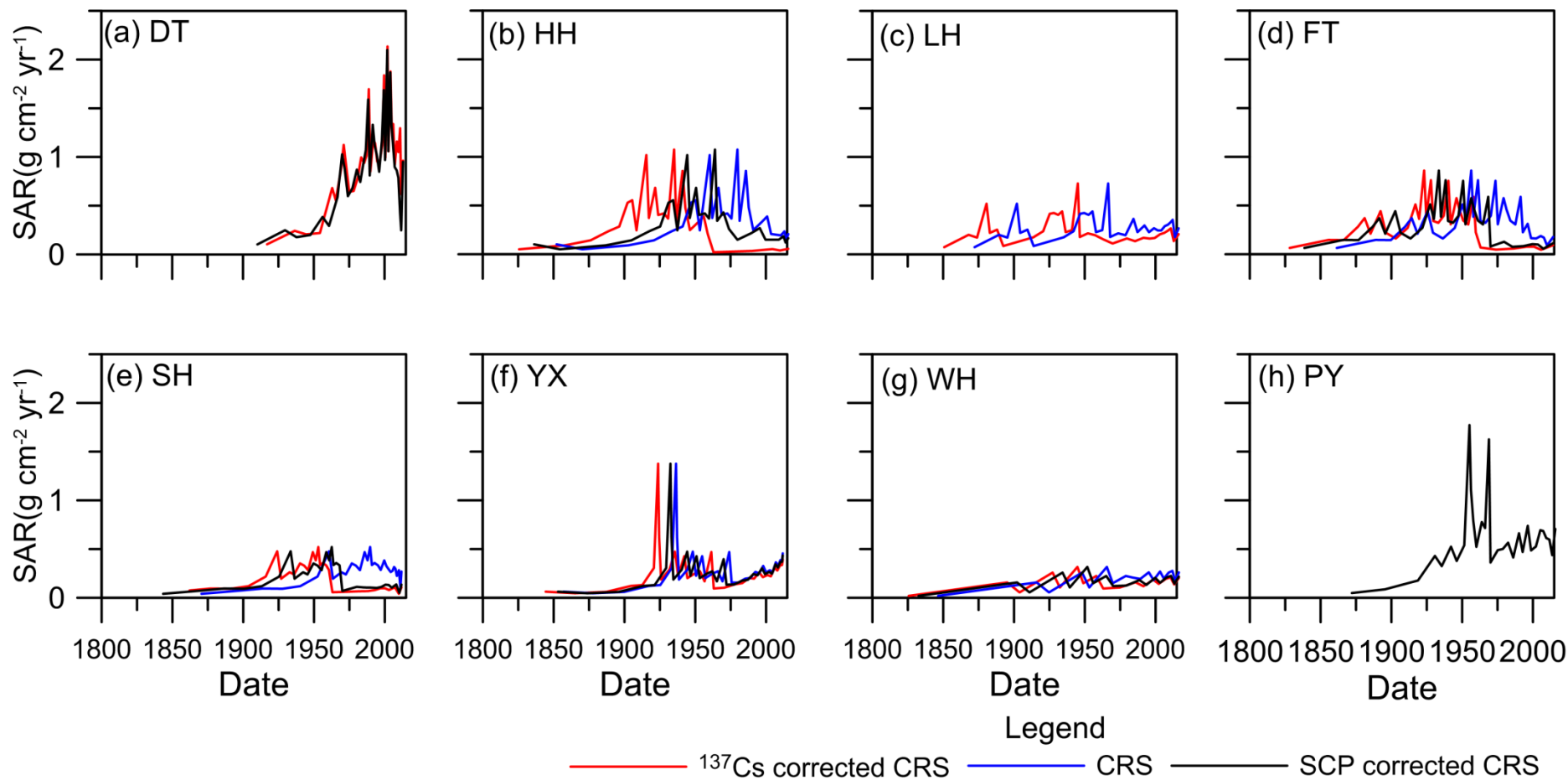
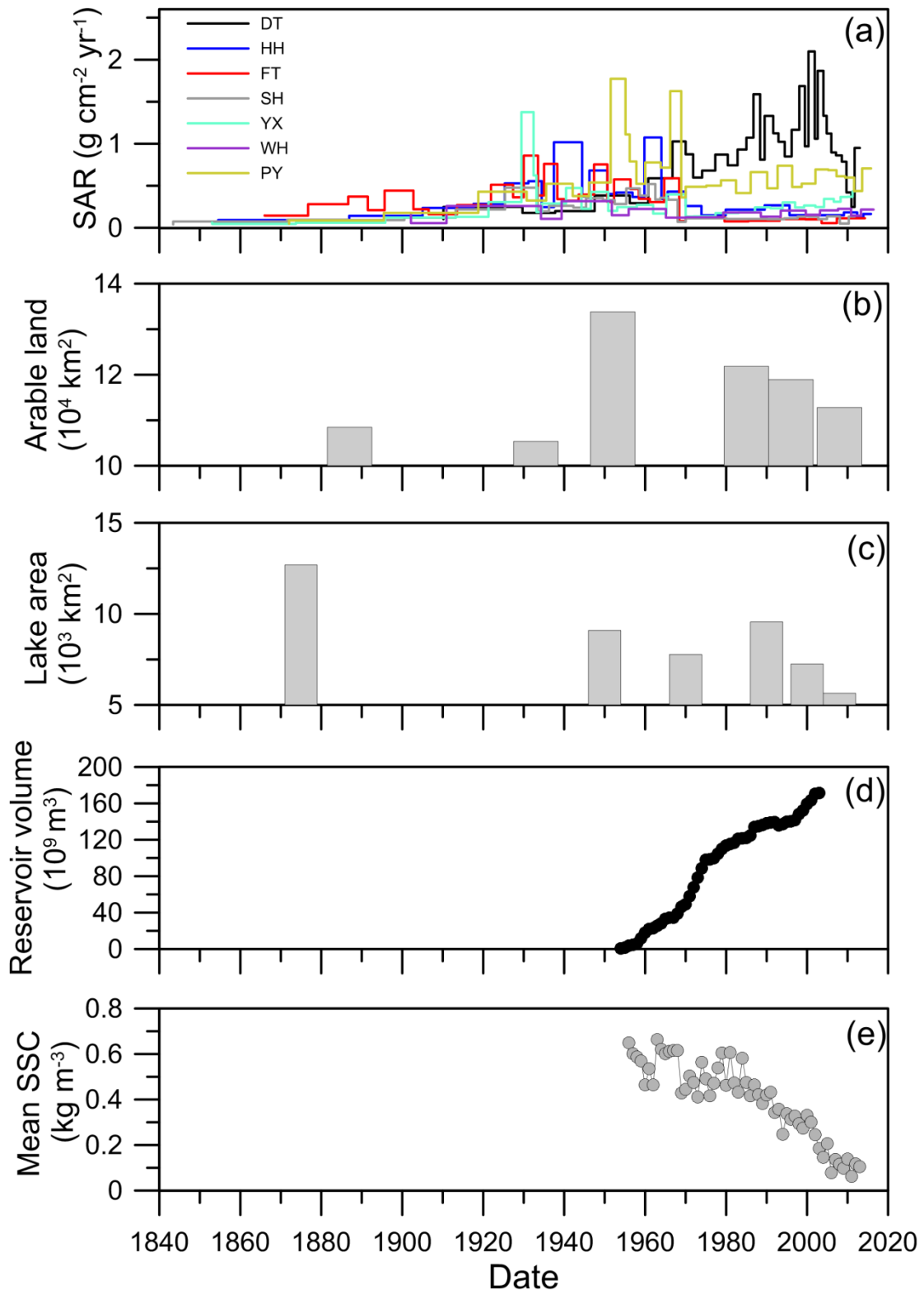


Figure 9



1  
2  
3

Figure 10